Supplemental Document

optica

Tensorial phase control in nonlinear meta-optics: supplement

Carlo Gigli,[1] Giuseppe Marino,[1] Alberto Artioli,[2] Davide Rocco,[3,4] Costantino De Angelis,[3,4] Julien Claudon,[2] Jean-Michel Gérard,[2] and Giuseppe Leo[1,*]

[1] *Matériaux et Phénomènes Quantiques, Université de Paris, Paris, France*
[2] *Univ. Grenoble Alpes, CEA, IRIG-PHELIQS, Grenoble, France*
[3] *Department of Information Engineering, University of Brescia, Brescia, Italy*
[4] *INO−CNR, Via Branze 38, 25123 Brescia, Italy*
[*] *Corresponding author: giuseppe.leo@u-paris.fr*

Supplement DOI: https://doi.org/10.6084/m9.figshare.13567760

Parent Article DOI: https://doi.org/10.1364/OPTICA.413329

Supplementary Material

Carlo Gigli[1], Giuseppe Marino[1], Alberto Artioli[2], Davide Rocco[3,4], Costantino De Angelis[3,4], Julien Claudon[2], Jean-Michel Gérard[2], and Giuseppe Leo[1,*]

[1] Matériaux et Phénomènes Quantiques, Université de Paris, Paris, France
[2] Univ. Grenoble Alpes, CEA, IRIG, PHELIQS, 38000 Grenoble, France
[3] Department of Information Engineering, University of Brescia, Brescia, 25123, Italy
[4] INO−CNR, Via Branze 38, 25123 Brescia, Italy

Contents

1. Isolated resonators and array properties

In order to ensure that the optimized meta-atoms are optically uncoupled, we first computed the emission properties from isolated resonators. The electric near fields were computed in an analogous way as reported in Section 4 of the manuscript. Here perfectly matching conditions were imposed all around the resonator, instead of periodic boundary conditions. In order to easily compare final results, we set the same phase for the background field. Using near-to-far-field transformations [S1], we computed the y component of SH electric far-field along z. Its amplitude and phase are reported on the left-most side of Figure S1. Then, we considered periodic structures with decreasing unit-cell size Λ. Figure S1 highlights that isolated resonator properties are progressively lost for $\Lambda < 900$ nm, due to inter-particle coupling. Thus, the choice $\Lambda = 900$ ensures both the finest achievable phase sampling for such geometry and a LUT whose properties stay valid for any arrangement of nanoresonators.

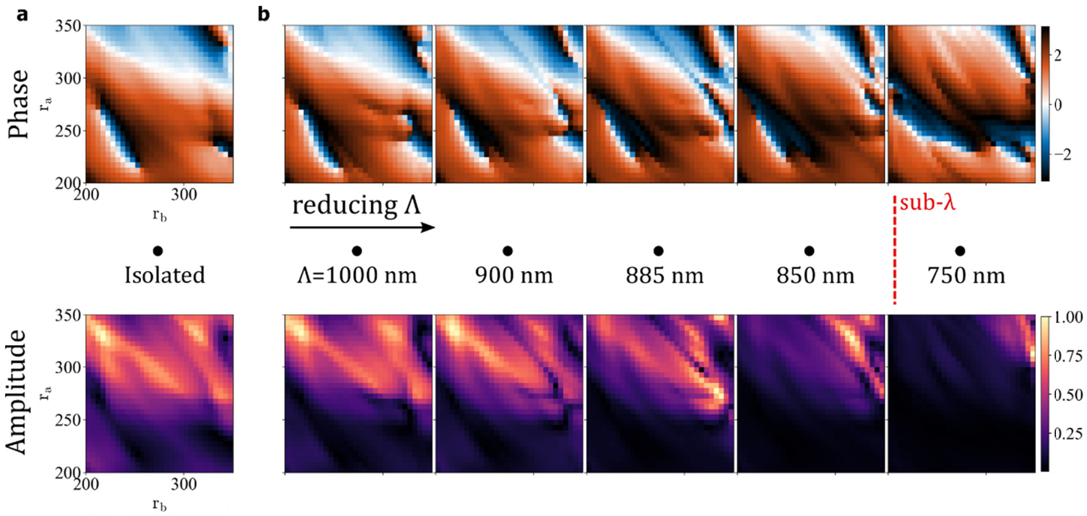

Figure S1. Top: Phase of the SHG signal from isolated (a) and arrayed (b) nanoresonators with the same geometry as sketched in the Figure 1a. Bottom: Same as (Top) for the SHG amplitude, which is normalized to its maximum in each panel. The two plots display the y component of SHG far-field along z. In (b) the unit-cell size decreases from the left to the right and the red dashed line shows the sub-λ threshold at SH.

2. Lookup table calculation

The numerical calculations described in Section 4 of the manuscript allow to predict the SH far-field properties from each meta-atom. To design a metasurface for phase encoding, we extracted the amplitude and phase of SH emission into the 0th diffracted order. According to section S2, Λ was chosen just above the sub-wavelength threshold at SH. To make sure that most of the emitted power is funneled into the 0th-diffracted order and the presence of 1st diffraction order can be considered as a perturbative contribution, the LUTs of Figure 3a were complemented by the calculation of the main SHG lobe direction, see Figure S2, We considered in this case the weighted emission direction from the normal expressed as $\bar{\theta}_{SH} = \sum|A_i|^2\theta_i/\sum|A_i|^2$, where A_i is the amplitude of the electric field radiated at angle θ_i.

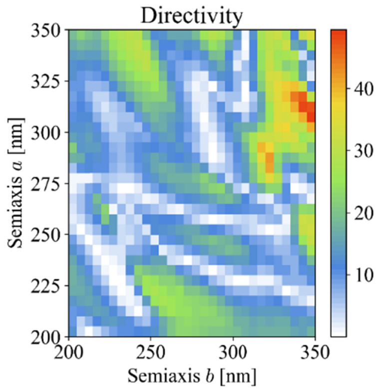

Figure S2. Average radiation angle of SH y-polarized component vs. the meta-atom geometry.

The response of the metasurface can be rewritten as the product between the emission from the meta-atom and the array factor [S2]. When the emission from the meta-atom is highly directional and close to the normal, most of the power at SH funnels into the 0^{th} diffracted order, see Figure S3.

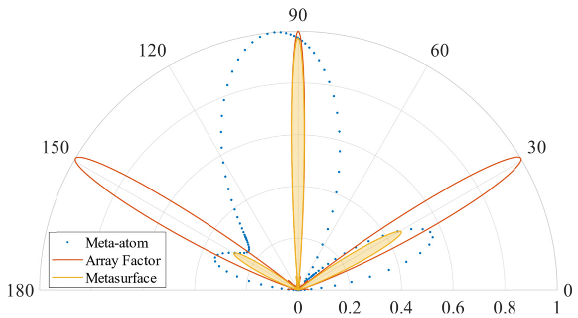

Figure S3. SHG from a meta-atom modulated by the array factor. Blue dots: radiation pattern at SH in forward direction from one of the meta atoms used for the beam steering device. Red line: array-factor of a grating with periodicity $\boldsymbol{\Lambda = 900\ \mathrm{nm}}$ and total size $\boldsymbol{70\ \mu\mathrm{m} \times 70\ \mu\mathrm{m}}$. Yellow area: product between the two, showing a main lobe at the 0^{th} diffracted order and two smaller lobes at large angles.

The algorithm to identify the elementary building blocks for wavefront shaping roots on two simultaneous optimizations: 1) The resonators generate a second harmonic with the same maximized amplitude at normal direction and phases scanning uniformly the $[0,2\pi]$ range, 2) the emission pattern from the meta-atom exhibits a maximum close to the normal. We therefore iteratively defined an amplitude mask to filter out just the resonators emitting SH with amplitude in the range $[A_i - \varepsilon, A_i + \varepsilon]$, with A_i the target amplitude for i^{th} iteration and ε a tolerance factor. We furtherly selected from this set just the resonators with a radiation lobe at $\theta < \theta_{Max}$, with θ_{Max} the maximum accepted deviation from the normal. We defined at this stage an error function e between the phase profile to implement φ_T and the real phase profile φ_R obtained with the subset of selected resonators:

$$e = \sum_i [\varphi_T(i) - \varphi_R(i)]^2$$

Finally, we minimized e and maximized the amplitude A_i. For a sawtooth phase profile with $N = 8$ elements between $[0,2\pi]$, $\varphi_T(i) = 2\pi(i - 1/2)/N$ and the optimized value for the amplitude filter was 63% of maximum amplitude. The filtered lookup table of Figure 2 is reported in Figure S4.

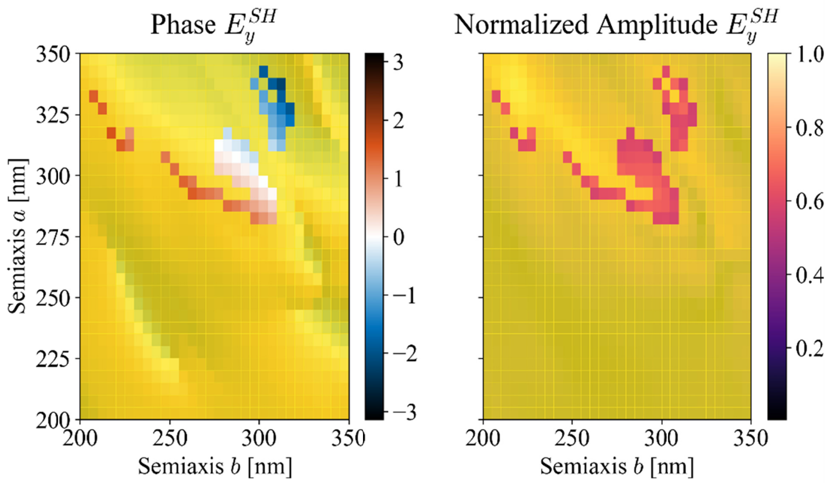

Figure S4. Lookup tables after filtering process. The selected geometries exhibit the same emission amplitude, a main radiation lobe close to the normal and a phase in the whole range $[\mathbf{0}, \mathbf{2\pi}]$.

The SH far-field patterns for the 8 structures of Figure 4 in the main text are reported in Figure S5.

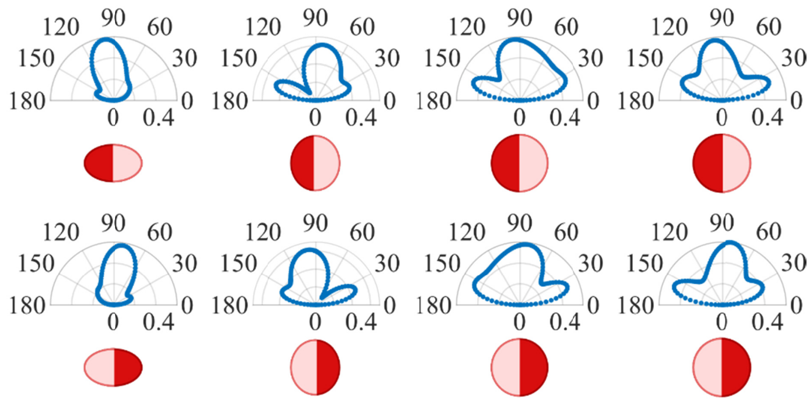

Figure S5. SH radiation pattern in the *xz* plane for the 8 chosen structures for beam steering in Figure 4. The *y*-polarized electric field is considered.

2.1 Lookup table validity

The LUT predictions were verified by the beam-steering metasurface of Figure 4. The near fields of the 8 isolated meta-atoms, as predicted from LUT calculation, were compared with the fully numerical model of a super-cell including the same 8 resonators, by imposing periodic conditions at the edges of the super-cell. Results for the main field components at FF and SH are reported in Figure S6.

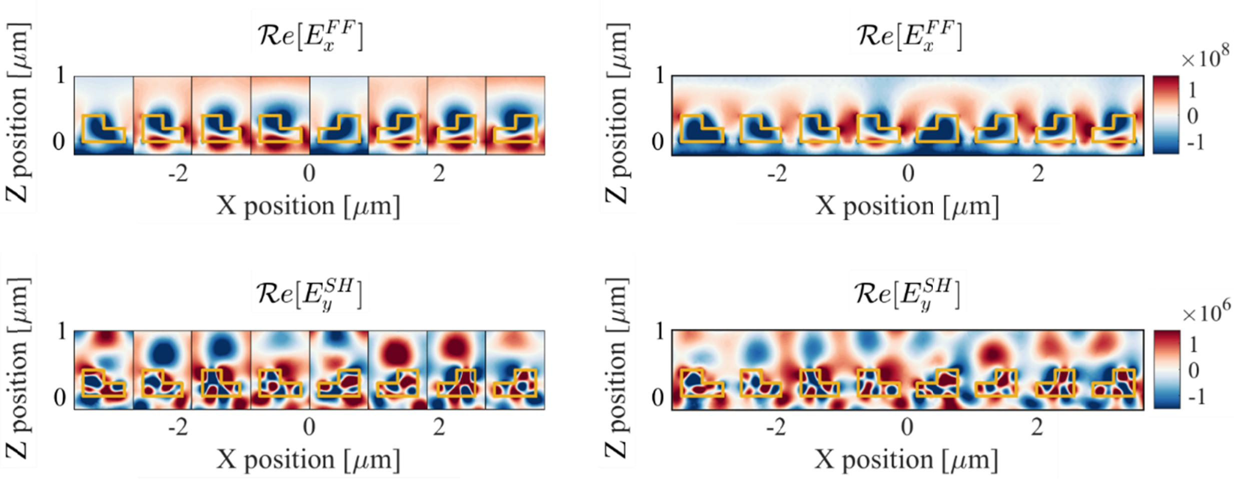

Figure S6. Comparison between LUT predictions (left) and supercell (right) for the steering device in Figure 4 in the *xz* plane. Top: total electric-field x component at FF (an intensity $\boldsymbol{I_0 = 1\mathrm{GW/cm^2}}$ was considered in the calculations). Bottom: electric-field *y* component at SH.

The former takes into account the interaction of neighboring resonators with different geometries, and it is the same configuration used to compute the numerical predictions in Figure 4. The comparison between the two shows just minor differences. Finally, the reconstruction of a continuous wavefront in the near-field was examined considering a larger volume along z. Figure S7 confirms that a tilted continuous wavefront with $\theta_B \sim 6.2°$ from the normal is retrieved, at a distance of about $13\lambda_{SH}$ from the metasurface.

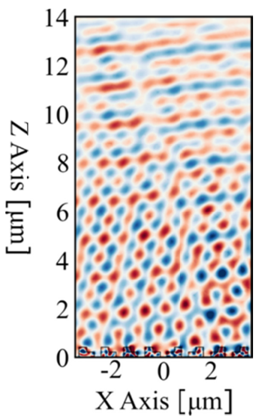

Figure S7. Electric near-field y component in a supercell made of 8 resonators and designed to steer the SHG beam by $\boldsymbol{6.2°}$. The plot reports the same simulation results as in bottom right of Figure S6, but in a larger supercell along *z*, so as to show the reconstruction of a continuous wavefront.

3. Sample fabrication

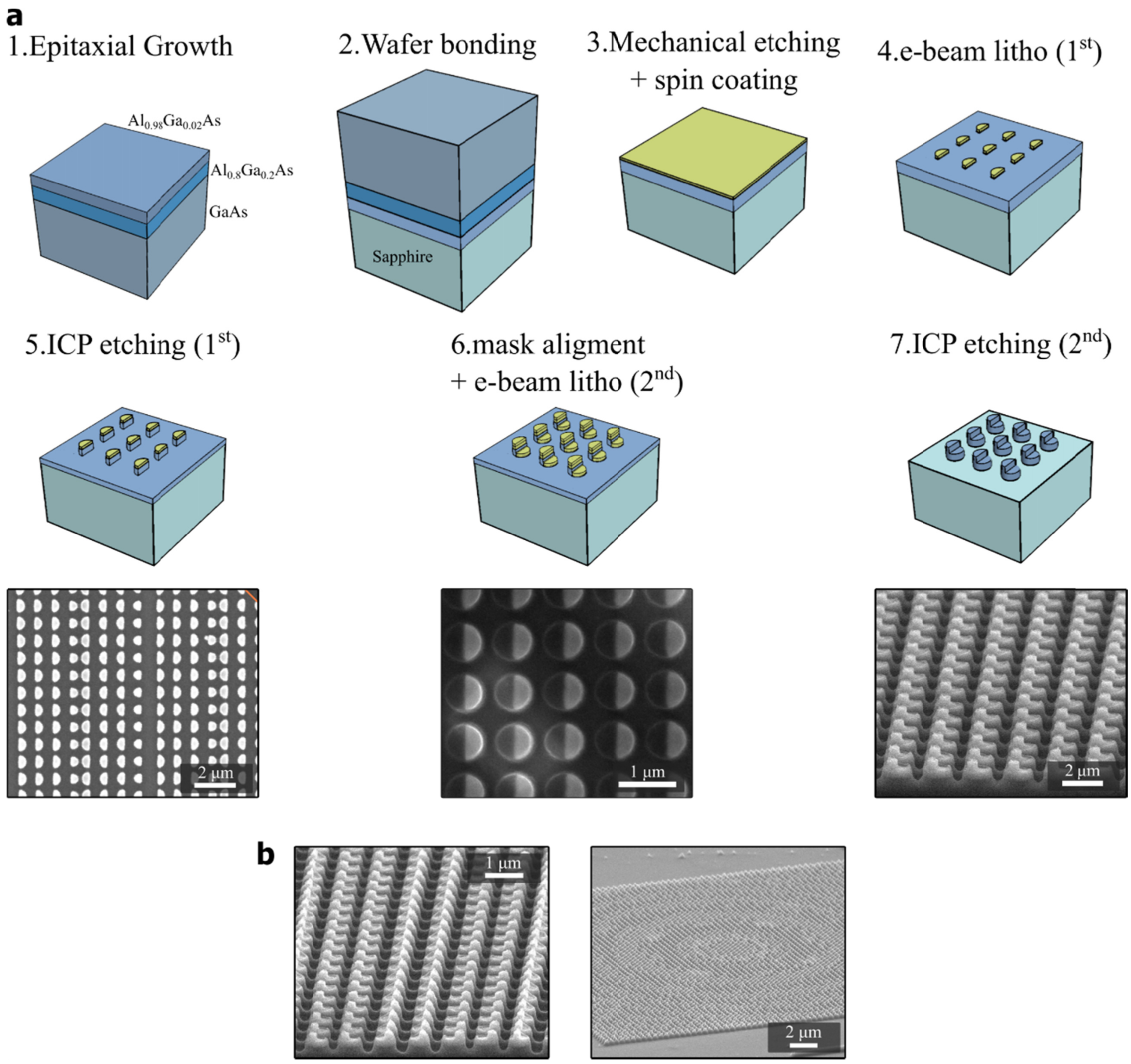

Figure S8. (a) Nanochairs-on-sapphire fabrication, with steps 5-7 being complemented by SEM images. (b) SEM views of nonlinear meta-grating (left) and meta-lens (right).

Figure S8 depicts the main technological steps to realize the nanochair structures which we detail in the following:

1. Fabrication started from a molecular beam epitaxy growth of 500-nm-thick $Al_{0.8}Ga_{0.2}As$ sacrificial layer on a (100) GaAs substrate, followed by 400-nm-thick $Al_{0.18}Ga_{0.82}As$ layer which constituted the future body of the nanochairs.
2. The epitaxial growth was then glued on a sapphire host substrate with a flip-chip process.
3. GaAs substrate and the sacrificial layer were thus removed by mechanical and selective chemical etching. In particular, the presence of this latter layer allowed to leave only the 400-nm-thick $Al_{0.18}Ga_{0.82}As$ as a mirror-flat surface. Man2403 negative resist was spin coated on the sample, assisted by Ti-Prime adhesion promoter. On top of this, a conductive polymer (Electra92) was spun to avoid electron charging during lithography.
4. The first half of the chair structure, as well as alignment marks for every metasurface, were patterned by e-beam lithography with an accelerating voltage of $\mathbf{20\ kV}$ and exposure dose of $\mathbf{120\ \mu C/cm^2}$.
5. A first ICP-RIE dry etching with $SiCl_4$ transferred the first half of cylinder pattern to the AlGaAs layer. In particular, in situ interferometry enabled to accurately control the etching depth, ensuring to stop after $\mathbf{200\ nm}$ of $Al_{0.18}Ga_{0.82}As$ were removed. An SEM image after this step is reported in the inset of Figure S8.
6. We performed a second e-beam lithography, aligned with the previously designed marks, to pattern the second half of the nanochairs. The same settings and the same resist were used. An SEM image showing the alignment precision is reported in the inset of Figure S8.
7. The fabrication was completed with a second ICP etching, with the same characteristics as the former one, and plasma oxygen to remove Man resist.

4. SHG experimental characterization

4.1 Experimental setup

The nonlinear optical characterization was performed with a home built horizontal microscope, see Figure S9. The pulsed light source, detailed in Section 4, was focused by a plano-convex lens with focal distance 400 mm on the back-focal plane of a 10X microscope objective with NA $= 0.2$. In this configuration a collimated beam could be ensured on the object plane [S3]. The excitation power was measured by an InGaAs photodiode (Newport 818-IG) before the objective, and the input polarization was set by an achromatic half-wave plate (Thorlabs AHWP10M-1600) and optimized with a wire-grid polarizer (Thorlabs WP25M-UB) placed on the object plane. A short-pass dichroic mirror (Thorlabs DMSP950) was used along the excitation line to collect the SH emitted in backward direction. The SH signal emitted in forward direction was collected by a 100X objective with NA $= 0.8$ (Olympus LMPLFLN 100X) placed on an automized stage to scan along the z direction and acquire images at different object planes. For back focal plane imaging a Bertrand lens with focal distance 200 mm was placed along the collection path.

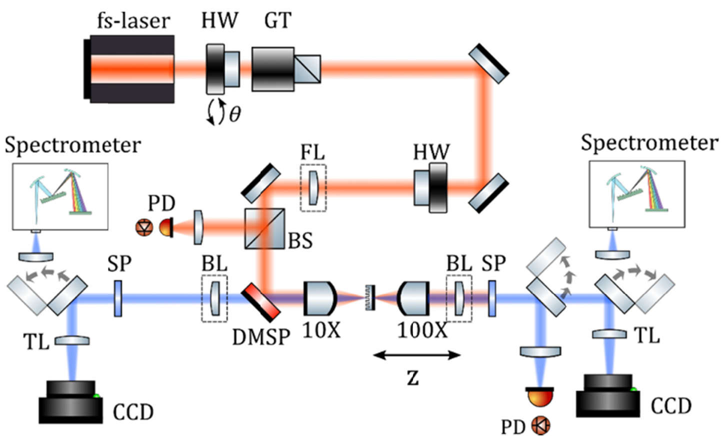

Figure S9. Experimental setup used for the characterization of nonlinear metasurfaces: pump beam (red), plano-convex lens (FL). InGaAs power meter (PD), half-wave plate (HW), Bertrand lenses (BL), dichroic mirror (DMSP). Pump power is controlled by an automatized half waveplate (HW) combined with a Glan-Taylor polarizer (GT). Short pass filter (SP, Thorlabs FESH850) were placed along detection path to remove pump beam. Collected signals were characterized either with a CCD camera, a fiber-coupled spectrometer, or a Si power meter (PD, Newport 818-SL).

The size of the collimated beam on the object plane was characterized by knife edge measurement. The experience was repeated at different positions between the two objectives and the collected signal was fitted assuming a gaussian beam profile. The extracted waist sizes at different positions are reported in Figure S10.

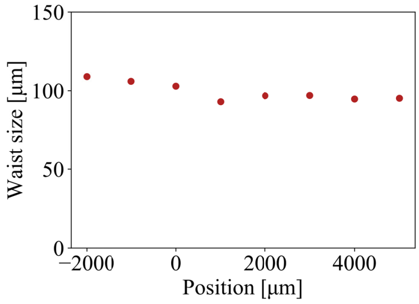

Figure S10 Knife-edge measurements at different positions between the two objectives. z=0 refers to the focal plane of 10X objective. The reported waists are extracted from the measured power during knife-edge characterization fitted by an erf function.

4.2 SH characterization

SH emission was characterized spectrally to verify the purity of the signal and confirm the absence of two-photon luminescence from the substrate. A Qmini fiber coupled spectrometer (Broadcom) was used for the measurement and the result is reported in Figure S11. The Gaussian fit is peaked at 774.6 nm with FWHM = 6.5 nm.

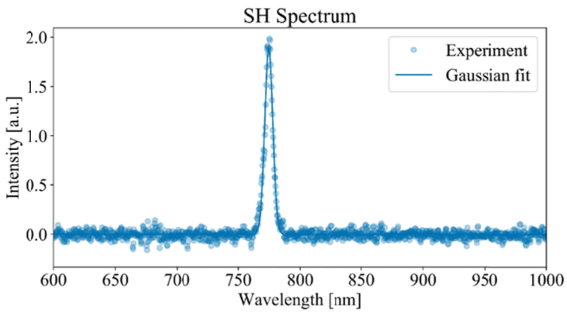

Figure S11 Nonlinear emission spectrum from an array of identical resonators.

4.3 Experimental SHG efficiency

Finally, SHG was experimentally tested by extracting the relation between SH and FF power. Figure S12 reports the $\bar{P}_{SH}/\bar{P}_{FF}$ ratio for a constant phase profile (Figure 4c top), the beam steerer (Figure 4c bottom) and meta-lens (Figure 5). The three results consistently show that SHG efficiency is independent of the specific phase profile.

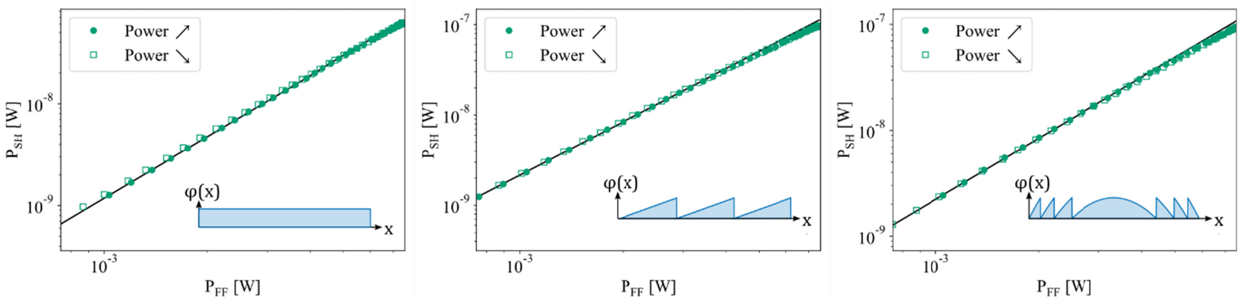

Figure S12. Measured SH vs. FF time-averaged power for three phase profiles, from left to right: a uniform meta-surface, a meta-grating, and a meta-lens. Full circles and empty squares refer to increasing or decreasing FF power, respectively, proving that the sample does not undergo irreversible processes when illuminated at high power.

The average interpolation coefficient is 1.96$\pm$0.04 in all cases, i.e. very close to what is expected for SHG. The maximum recorded conversion ratio $\bar{P}_{SH}/\bar{P}_{FF}$ was 1.3×10^{-5} for an average pump power $\bar{P}_{FF} = 7.4$ mW.

We evaluated the intrinsic conversion efficiency η_{SHG} considering the power generated by a single resonator in the metasurface $P_{SH}^{res} = P_{SH}/N$ with N the number of resonators in the metasurface normalized by the peak power impinging on a single resonator:

$$P_{FF}^{res} = I_{FWHM} \cdot (\pi r_a r_b) = \frac{\overline{P_{FF}}}{R_{dic}T_{obj}(\tau_p\, RR)} \frac{\pi ab}{\pi w_0^2}$$

where I_{FWHM} is the spatially-averaged intensity impinging on the metasurface, a and b are the resonator semiaxes, $\bar{P}_{FF}$ the time-averaged power measured by the power meter, while R_{dic} and T_{obj} are the dichroic reflectivity and objective transmittivity at $\lambda = 1550$ nm, respectively. Finally, τ_p and RR are the pump pulse width and repetition rate, respectively. Under these assumptions we finally extracted a SHG efficiency $\eta_{SHG} \sim 9.3 \times 10^{-7} W^{-1}$.

4.4 Spectral response

The resonating behavior of nanochair meta-atoms was investigated evaluating SHG efficiency vs. pump wavelength. The spectral response is shown in Figure S13, highlighting a resonant peak at $\lambda_{FF} = 1570$ nm with FWHM≈65 nm, revealing a Q-factor around 23, mainly determined by resonances at SH.

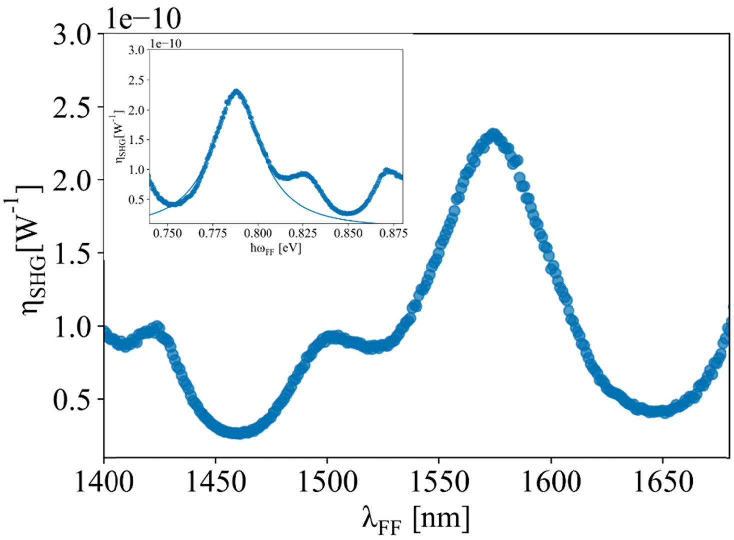

Figure S13. Spectral response of SHG from a uniform metasurface of identical nanochairs. Inset: dependence as a function of pump photon energy. The Lorentzian fit reveals a resonant peak at 0.788 eV (1574 nm) with a full-width-half-maximum of 0.033 eV (65 nm).

The shift of 20 nm from the optimized wavelength $\lambda_{FF} = 1550$ nm is not surprising as the constant amplitude condition mentioned in section "Lookup Table calculation" requires that all the selected meta-atoms exhibit the same SHG intensity at design working wavelength, but it does not impose that this should correspond to the maximum of resonance peak for all of them.

4.5 Beam steerer spectrum

Figure S14a reports the experimental behavior of the meta-grating vs. FF wavelength, i.e. a more comprehensive study than the bottom panel of Figure 4c in the manuscript (which reports this efficiency just at the optimized wavelength $\lambda_{FF} = 1550$ nm). It displays the power funneled into the 15 diffraction orders within the numerical aperture of the 100X objective in Figure S9 in the spectral region $\lambda_{FF} \in [1450 - 1650]$ nm. For the optimized wavelength $\lambda_{FF} = 1550$ nm, SHG is deflected into the first diffracted order at 6.2°. Figure S14b highlights the diffraction efficiency of the first diffracted order as a function of the FF wavelength, which results to be around 47%

and remains larger than 40% in the range $\lambda_{FF} \in [1540 - 1600]$. Although at larger wavelengths diffraction efficiency increases over 70%, we do not consider this spectral region as a useful working range as SHG efficiency drops, as shown by Figure S13.

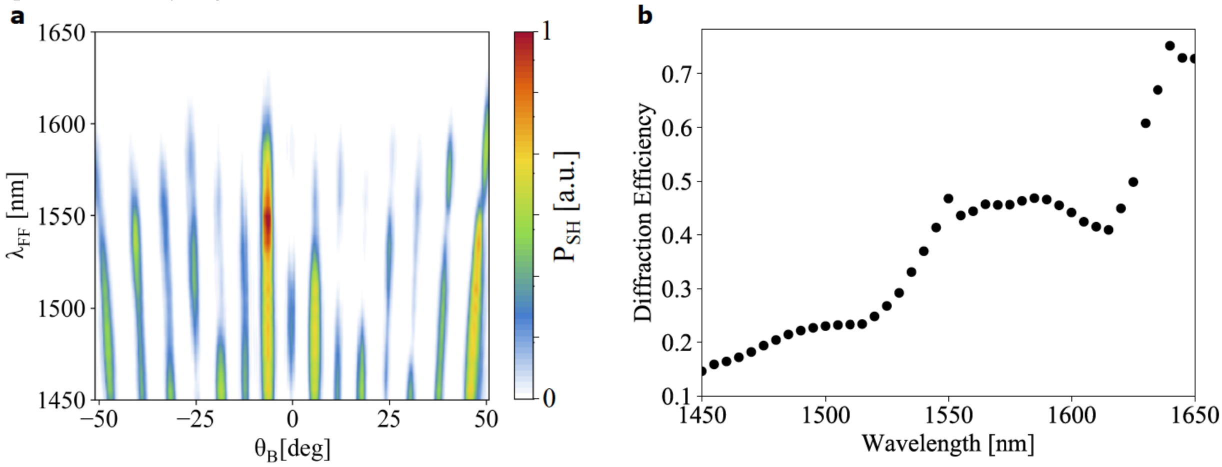

Figure S14. a) Spectral response of the beam steerer SH efficiency imaged in the Fourier plane vs. deflection angle θ_B; b) diffraction efficiency for the 1st diffraction order as a function of the incident wavelength.

4.6 Meta-lenses characterization

The focusing behavior of the designed meta-lenses was probed by scanning the SH signal at different image planes. As shown in Figure S9, the collection objective is mounted on a motorized stage (Thorlabs Z812B) which allows to reconstruct the profile of the focused beam. In order to extract an accurate spatial information, the images on the camera were calibrated through a 20 µm-long reference mark fabricated on the same sample and corresponding to 300 pixels on the CCD device, see Figure S15. We therefore estimate a spatial resolution of 0.07 µm.

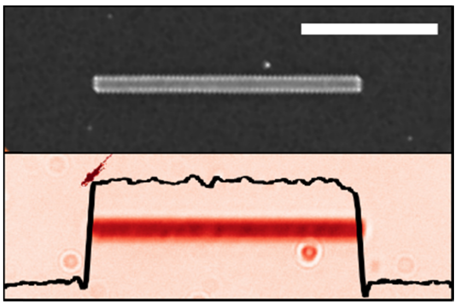

Figure S15. Reference mark for spatial calibration. Top: SEM image, the white scale bar equals to 10 µm. Bottom: image acquired by CCD camera with 100X objective. The black curve represents the sum of pixels along vertical direction.

We acquired an image every micrometer, and at each position z on the optical axis we implemented a numerical knife-edge measurement extracting the waist $w(z)$. The fit result assuming a Gaussian beam profile is reported in Figure S16a at two different positions. In this way the beam waist profile $w(z)$ was extracted and fitted with the hyperbolic relation:

$$w(z) = w_0 \sqrt{1 + \left(\frac{z - z_0}{z_R}\right)^2}$$

Where w_0 denotes the beam waist at focal point z_0 and $z_R = \pi w_0^2/\lambda$ the Rayleigh range. At $z = z_0$ the acquired image exhibits the characteristic Airy pattern of diffraction limited spots with an intensity profile of the type:

$$I(x) = I_0 \left[\frac{2J_1\left(\frac{2\pi}{\lambda} xNA\right)}{\frac{2\pi}{\lambda} xNA} \right]^2$$

with NA the numerical aperture of the designed lens. The first minimum of Airy function is at $x = 1.22\lambda/2NA$. In order to extract an expected value for the focused spot size we approximated the Airy pattern with a Gaussian distribution $I(x) = I_0{}' \exp(-x^2/2\sigma_{RMS})$. One finds that the root mean square spot size corresponds to $\sigma_{RMS} \sim 0.21\lambda/NA$ or equivalently $w_0 \sim 0.42\lambda/NA$. In turn for the two designed lenses with NA=0.2 and 0.5, the expected beam waists at focal distance are $w_0 = 1.63$ µm and 0.66 µm, respectively. The experimentally fitted values are 1.75 µm and 0.65 µm, in agreement with those expectation considering the spatial resolution of the experimental optical system. A 3D reconstruction of the SH focusing beam is reported in Figure S16b-c.

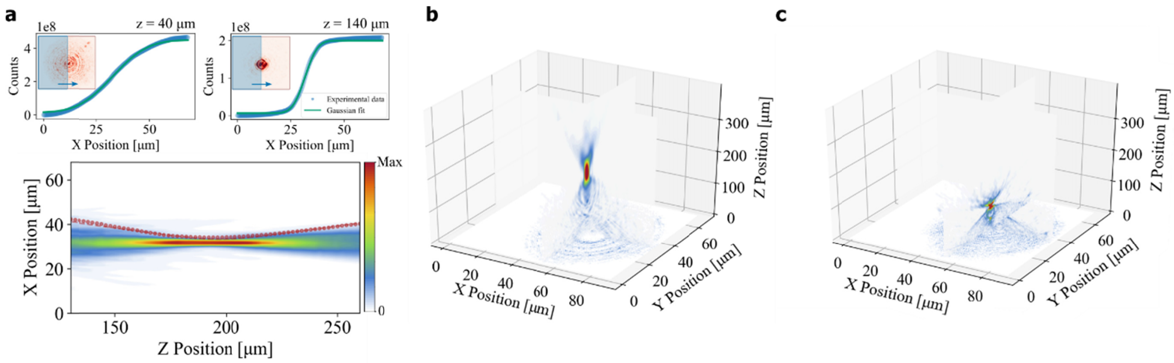

Figure S16. Meta-lens characterization. (a)Top: numerical knife-edge measurement at two distances $\boldsymbol{z = 40}$ **µm** and **140 µm** from the metasurface along optical axis. The power is integrated along x direction (blue dots) and fitted with a Gaussian (green solid line) to extract the waist size. Bottom: beam waist reconstruction. (b-c) SH focused beam reconstruction in the 3 planes $\boldsymbol{xy}$, $\boldsymbol{xz}$ and $\boldsymbol{yz}$ for the meta-lenses with NA=0.2 (b) and 0.5 (c).

Furthermore, in order to evaluate the diffraction efficiency of the two meta-lenses we computed the ratio between SHG at focal point $z = f$ and at metalens plane $z = 0$. We added a spatial filtering at focal plane with the aim to remove possible out-of-focus contributions, see Fig. S17.

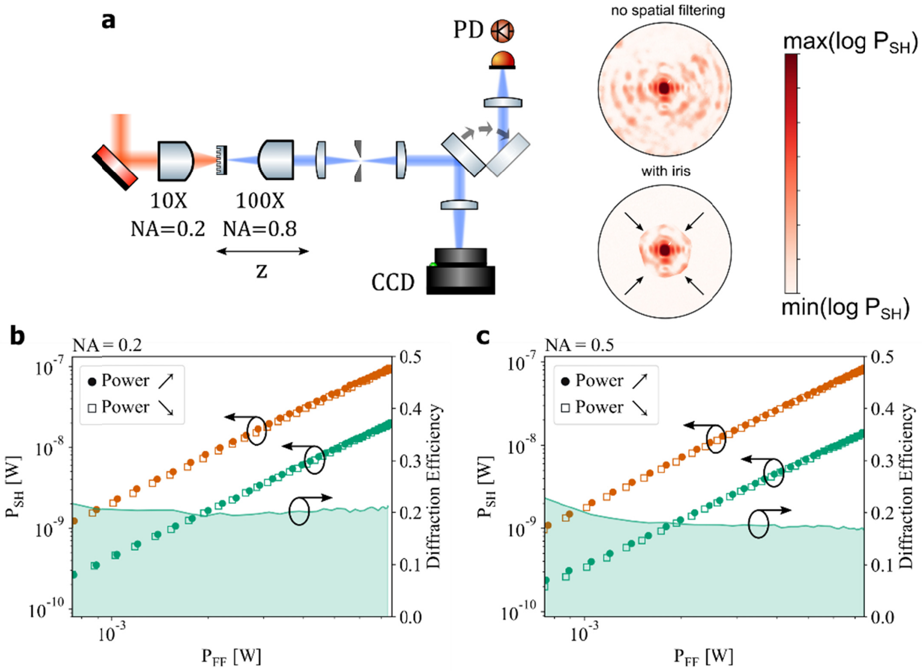

Figure S17. Experimental study of the nonlinear meta-lenses efficiency. (a) Spatial filtering along collection path to remove out-of-focus contributions. An intermediate image plane is created with two plano-convex lenses (Thorlabs LA4725-B-ML) and the interesting region is selected with a variable size aperture. (b-c) Total (orange) and focused (green) SHG varying pump power for designed NA=0.2 (b) and 0.5 (c). Right axes display the ratio between the two, determining the diffraction efficiencies of the two devices.

5. Efficiency comparison for nonlinear beam shaping

Here we report a table comparing the conversion efficiency for relevant publications on nonlinear beam shaping. Most of them refer to $\chi^{(3)}$ metasurfaces. To the best of our knowledge, Ref. [19] in main text is the sole reported $\chi^{(2)}$ metasurface for phase encoding to date. The impact of our work is highlighted by the comparison of the normalized nonlinear efficiencies. All the references in the table resort to the main text numbering.

Ref.	Type	NL efficiency	Normalized NL efficiency	P_{FF}	$I_{FF}(FWHM)$
[17]	Gold - $\chi^{(3)}$	N/A	N/A	1.9 kW	9.3 MW/cm^2
[18]	Gold - $\chi^{(3)}$	$P_{TH}/P_{FF} = 10^{-8}$	$P_{TH}/P_{FF}^3 = 2.5 \times 10^{-22}$ W^{-2}	6 MW	20 GW/cm^2
[19]	Gold - $\chi^{(2)}$	$P_{SH}/P_{FF} = 10^{-11}$	$P_{SH}/P_{FF}^2 = 6 \times 10^{-16}$ W^{-1}	18 kW	0.22 MW/cm^2
[22]	Silicon - $\chi^{(3)}$	$P_{TH}/P_{FF} = 10^{-6}$	$P_{TH}/P_{FF}^3 = 9 \times 10^{-16}$ W^{-2}	33 kW	N/A
[23]	Silicon - $\chi^{(3)}$	$P_{TH}/P_{FF} = 10^{-6}$	$P_{TH}/P_{FF}^3 = 6 \times 10^{-16}$ W^{-2}	42.3 kW	0.75 GW/cm^2
[24]	Silicon - $\chi^{(3)}$	$P_{TH}/P_{FF} = 10^{-6}$	N/A	N/A	33 GW/cm^2
This work	AlGaAs - $\chi^{(2)}$	$P_{SH}/P_{FF} = 1.3 \times 10^{-5}$	$P_{SH}/P_{FF}^2 = 2.8 \times 10^{-10}$ W^{-1}	47 kW	0.14 GW/ cm^2

References

S1. J. Yang, J. P. Hugonin, and P. Lalanne, "Near-to-Far Field Transformations for Radiative and Guided Waves," ACS Photonics **3**(3), 395–402 (2016).

S2. R. C. Hansen, *Phased Array Antennas*, Second Edi (Wiley, 2009).

S3. P. Hauer, J. Grand, A. Djorovic, G. R. Willmott, and E. C. Le Ru, "Spot Size Engineering in Microscope-Based Laser Spectroscopy," J. Phys. Chem. C **120**(37), 21104–21113 (2016).